Ultrastructural Characterization of Arterivirus Replication Structures: Reshaping the Endoplasmic Reticulum To Accommodate Viral RNA Synthesis

Kèvin Knoops,[a,b]* Montserrat Bárcena,[a] Ronald W. A. L. Limpens,[a] Abraham J. Koster,[a] A. Mieke Mommaas,[a] and Eric J. Snijder[b]

Electron Microscopy Section, Department of Molecular Cell Biology,[a] and Molecular Virology Laboratory, Department of Medical Microbiology, Center of Infectious Diseases,[b] Leiden University Medical Center, Leiden, The Netherlands

Virus-induced membrane structures support the assembly and function of positive-strand RNA virus replication complexes. The replicase proteins of arteriviruses are associated with double-membrane vesicles (DMVs), which were previously proposed to derive from the endoplasmic reticulum (ER). Using electron tomography, we performed an in-depth ultrastructural analysis of cells infected with the prototypic arterivirus equine arteritis virus (EAV). We established that the outer membranes of EAV-induced DMVs are interconnected with each other and with the ER, thus forming a reticulovesicular network (RVN) resembling that previously described for the distantly related severe acute respiratory syndrome (SARS) coronavirus. Despite significant morphological differences, a striking parallel between the two virus groups, and possibly all members of the order *Nidovirales*, is the accumulation in the DMV interior of double-stranded RNA, the presumed intermediate of viral RNA synthesis. In our electron tomograms, connections between the DMV interior and cytosol could not be unambiguously identified, suggesting that the double-stranded RNA is compartmentalized by the DMV membranes. As a novel approach to visualize and quantify the RNA content of viral replication structures, we explored electron spectroscopic imaging of DMVs, which revealed the presence of phosphorus in amounts equaling on average a few dozen copies of the EAV RNA genome. Finally, our electron tomograms revealed a network of nucleocapsid protein-containing protein tubules that appears to be intertwined with the RVN. This potential intermediate in nucleocapsid formation, which was not observed in coronavirus-infected cells, suggests that arterivirus RNA synthesis and assembly are coordinated in intracellular space.

L ipid membranes define the boundaries of all important cellular organelles, like mitochondria, the endoplasmic reticulum (ER), and the Golgi complex. They are also indispensable for the biochemical functions performed by these highly specialized microcompartments, which require both structural support and physical separation from the cytosol. Along the same lines, all positive-strand RNA (+RNA) viruses characterized to date induce the formation of dedicated membrane structures to support the cytoplasmic replication of their RNA genomes (9, 30, 35, 44). Apparently, the formation of these membranous compartments offers important functional and/or strategic benefits for the viral RNA-synthesizing machinery.

For a number of +RNA viruses, the continuous improvement of cryofixation methods and the advent of electron tomography (ET) have made important contributions to the visualization of their replication structures by offering better preservation (38, 46, 49, 52), higher resolution imaging, and the possibility of three-dimensional (3-D) ultrastructural analysis (18, 23, 25, 29, 65). Furthermore, immuno-electron microscopy (IEM) has been used to investigate the presence of viral replicase subunits, host cell markers, and viral RNA products in +RNA virus replication structures. The combination of these technical approaches established that the specific association of replicase proteins and newly synthesized viral RNA with these membrane compartments is a common feature of all +RNA virus models studied to date.

Recent ET-based studies provided valuable information about the 3-D ultrastructure of the replication structures formed by, e.g., the nodavirus Flock House virus (FHV) (25), severe acute respiratory syndrome coronavirus (SARS-CoV) (23), dengue and West Nile flaviviruses (18, 65), and rubella virus (15). Flock House virus generates small spherular invaginations of the mitochondrial outer membrane (25, 34) similar to those induced by alphaviruses in endosomal and lysosomal membranes (16). Electron tomography of flavivirus-infected cells demonstrated similar invaginations, but in this case, ER membranes serve as platforms for the biogenesis of the replication structures (18, 65). Moreover, flaviviruses induce a more extensive network of membrane structures that has been implicated in organizing the different stages of the replicative cycle in space and time (18, 21, 30, 36, 58, 65). The accumulation of different membrane structures, whose respective functional importance remains to be investigated, was also documented for picornaviruses (5, 6, 29, 38, 46, 57) and coronaviruses (7, 19, 22, 23, 54, 59). Members of the latter family induce typical double-membrane vesicles (DMVs) and also convoluted membranes (CM), which ET revealed to be part of a reticulovesicular network (RVN) of modified ER that is continuous with its membrane donor (23, 59).

Arteriviruses are only distantly related to coronaviruses. In spite of important differences in terms of genome size, virion

structure, and various other biological features (20), the two families have been united in the order *Nidovirales* based on striking similarities in genome organization and expression and the conservation of important replicase domains. The latter include similar membrane-spanning nonstructural proteins (nsps) that are thought to induce the formation of membrane structures with which viral RNA synthesis is associated. Also arterivirus-infected cells are characterized by the accumulation of double-membrane sheets and DMVs (41, 60), but the average diameter of the latter is about three times smaller than those induced by coronaviruses (100 versus 300 nm), and CM have not been observed. The biochemistry and molecular biology of the replication machinery of the arterivirus prototype equine arteritis virus (EAV) have been studied extensively in our laboratory (14, 50). The 5′-terminal open reading frames (ORFs) 1a and 1b in the 12.7-kb EAV genome encode the replicase polyproteins pp1a (1,727 amino acids [aa]) and pp1ab (3,175 aa), with the latter being a C-terminally extended version of the former that is derived from a ribosomal frameshifting mechanism. Three ORF1a-encoded protease domains mediate cleavage of the replicase polyproteins into at least 13 individual nonstructural proteins, which mostly accumulate in the perinuclear region of the infected cell. The key enzymes of the arterivirus replication and transcription complex (RTC), and also the most conserved replicase functions among nidoviruses, are encoded in ORF1b and include an RNA-dependent RNA polymerase (RdRp) (nsp9) and helicase (HEL) (nsp10). The ORF1a-encoded nsp2, nsp3, and nsp5 contain transmembrane regions that are believed to anchor the RTC to intracellular membranes and to transform them into DMVs (51). Expression of nsp2 and nsp3 induces the formation of very similar membrane structures, and these proteins were therefore proposed to direct membrane pairing and vesicle formation (42, 51). As in the case of mouse hepatitis virus (MHV) (22), *de novo*-made EAV RNA was found both associated with DMVs and in the surrounding cytosol (41).

In our quest to understand the structure and function of nidovirus RTCs and their supportive membrane structures, we have now extended our ultrastructural analysis to EAV-infected cells. A major advantage is that these samples can be processed for cryofixation (CF) without the need for a chemical prefixation, a biosafety prerequisite when working with SARS-CoV-infected cells. From a general point of view, cryoimmobilization is faster and has been shown to provide better morphology and improved membrane contrast in a large variety of specimens (39). Using direct CF and a combination of advanced microscopy techniques, we have performed an in-depth characterization of EAV-infected cells and established some striking parallels between arteriviruses and coronaviruses. For example, ET revealed that the EAV-induced DMVs are also interconnected and integrated into an RVN of modified ER. Again, colocalization of replicase products and double-stranded RNA (dsRNA) was limited, with the latter being present predominantly in the electron-dense cores of DMVs and the former mainly localizing to RVN membranes. Finally, we explored electron spectroscopic imaging (ESI) to visualize and quantitate the RNA content of individual replication vesicles, and we show that this technique may constitute a novel tool to study +RNA virus replication structures.

MATERIALS AND METHODS

Virus, cells, and antisera. A cell-culture-adapted derivative of the EAV Bucyrus isolate (11) was used to infect monolayers of Vero E6 cells grown in Dulbecco's modified Eagle's medium supplemented with 10% fetal calf serum. A multiplicity of infection of 10 and an incubation temperature of 39.5°C were used in all EAV infection experiments, and infection rates were routinely confirmed in immunofluorescence (IF) assays. Rabbit antisera recognizing the EAV replicase subunits nsp3 (41) and nsp9 (61) were described previously. Monoclonal antibodies (MAbs) against the EAV N protein (31) and dsRNA (MAb J2 [47, 64]) were also documented previously.

Immunofluorescence microscopy. Infected cells grown on glass coverslips were fixed with 3% paraformaldehyde in phosphate-buffered saline (PBS) at various time points after infection and were processed for IF microscopy essentially as described previously (60). Following permeabilization, single- or dual-labeling IF assays were carried out with rabbit antisera and/or mouse monoclonal antibodies, which were detected using appropriate indocarbocyanine (Cy3)-conjugated donkey anti-rabbit immunoglobulin (Ig) and Alexa Fluor 488 (Al488)-conjugated goat anti-mouse Ig secondary antibodies, respectively (Molecular Probes). To allow dual-labeling experiments with the nsp3 serum and a second rabbit antiserum recognizing a different nsp, an IgG fraction was isolated from the anti-nsp3 antiserum for direct coupling to Alexa Fluor 488, as described previously (49). Specimens were examined with a Zeiss Axioskop 2 fluorescence microscope (equipped with the appropriate filter sets, a digital Axiocam HRc camera, and Zeiss Axiovision 4.2 software [Carl Zeis and Microimaging]) or with a Leica SP5 confocal laser scanning microscope, using a pinhole size of 1 airy unit. Images were optimized and analyzed for colocalization with the WCIF version of ImageJ (http://www.uhnresearch.ca/facilities/wcif/imagej/). The Manders overlap coefficients were calculated as described by Li and coworkers (28).

Electron microscopy (EM). For ultrastructural morphological investigations, EAV-infected Vero E6 cells were fixed at various time points after infection. The procedures that were used for either chemical fixation or CF by plunge freezing have been described previously (23, 49). When high-pressure freezing (HPF) was applied, cell monolayers adhered to sapphire discs (Leica) were frozen using a Leica EM PACT2 high-pressure freezer. Freeze substitution (FS) was carried out in an automated FS system (Leica) using a medium consisting of 2% osmium tetroxide, 1% glutaraldehyde, and 10% H_2O in acetone. Samples were kept at -90°C for 9 h, after which the temperature was raised by 23.33°C/h to -20°C, at which temperature samples were kept for 1 h. Subsequently, the temperature was raised by 20°C/h to 0°C, and samples were kept at this temperature for 1 h. After washing with pure acetone at 0°C and room temperature, the samples were embedded in epoxy LX-112 resin. Thin sections were contrasted with uranyl acetate and lead citrate and subsequently viewed at 80 kV with a Tecnai 12 BioTwin transmission electron microscope (FEI Company).

For IEM, infected cell monolayers were cryofixed by HPF as described above, but FS was performed in anhydrous acetone containing 0.25% glutaraldehyde and 0.1% uranyl acetate for nsp and N protein labeling and 0.2% uranyl acetate and 1% methanol for dsRNA labeling. For the dsRNA labeling, prefixation with 3% paraformaldehyde in 0.1 M PHEM buffer [60 mM piperazide-1,4-bis (2-ethanesulfonic acid), 25 mM HEPES, 2 mM $MgCl_2$, 10 mM EGTA] was used, as it was found to improve labeling efficiency. During the FS step, samples were kept at -90°C for 72 h, after which the temperature was raised by 23.33°C/h to -20°C. After keeping the samples for 1 h at this temperature, the temperature was lowered by 20°C/h to -50°C. After washing with ethanol, samples were infiltrated with Lowicryl HM20 (Electron Microscopy Sciences) and polymerized under UV light at -50°C. Thin sections were labeled with the different primary antisera, which were detected with 10-nm protein A-gold particles. A bridging rabbit anti-mouse IgG antibody (DakoCytomation) was used when the primary antibody was a mouse monoclonal antibody. Grids were contrasted with uranyl acetate and lead citrate and subsequently viewed in a Tecnai 12 BioTwin transmission electron microscope at 80 kV. The specificity of immunolabeling was verified by comparing the amount of gold beads in the RVN/DMV-containing perinuclear area with those in equivalent areas of the nucleus, cytosol, extracellular space, and

mitochondrion-containing regions. For each labeling, using a Tecnai 12 BioTwin electron microscope running at 120 kV, overlapping high-magnification images containing at least three whole cells were acquired and merged into a single mosaic image by using homemade MatLab scripts (F. G. A. Faas, C. M. Avramut, A. J. Koster, and R. B. G. Ravelli, unpublished data). At low magnification (see Fig. 4E), specific areas of the cells in the mosaic images were selected and marked with a circle with a 10-μm² surface area. Subsequently, at a magnification at which the gold beads became visible, 15 such circles were used to quantify the amount of immunogold labeling in the extracellular space, nucleus, cytosol, mitochondrion-containing areas, and RVN-containing areas.

Electron tomography. Freeze-substituted infected cell samples, processed for morphological investigation by HPF as described above, were used to cut 200-nm-thick sections. Serial sections were placed side by side on Formvar/carbon-coated grids containing only 8 parallel bars, thus allowing analysis of the same cell in successive sections. To facilitate the image alignment required for tomogram production, a suspension of 10-nm gold particles was layered on top of the sections as fiducial markers. Dual-axis tomography was performed as described previously (23). To facilitate DMV quantification and size measurements in the tomograms, the central position of each DMV was marked in 3-D in the slice in which it had its largest diameter. By combining IMOD (see below) and Linux scripts, subvolumes of 250 by 250 by 10 pixels containing 10 sections around the DMV equator were extracted and binned 10 times in the z direction to obtain a 12-nm-thick slice. To calculate average sizes for DMVs and cores, the diameters in both the x and y directions were measured and averaged using ImageJ software.

Electron spectroscopic imaging. EAV-infected cells were high-pressure frozen at 8 h postinfection (p.i.) and freeze-substituted in 1% glutaraldehyde in acetone. Thin sections (60 nm) were cut and inspected in a Tecnai 12 BioTwin electron microscope to identify cytoplasmic areas that contained DMVs. Images at different magnifications were acquired at 80 kV, with the aim of retrieving the same area after transferring the specimen to a Tecnai 12 BioTwin electron microscope running at 200 kV, which was equipped with a postcolumn electron image filter (Gatan). Because of the significant contrast reduction at 200 kV, zero-loss images of the same cytoplasmic areas were recorded to obtain overview images. Next, pre- and post-edge images were acquired at an energy loss of 120 and 157 eV, respectively, with a slit width of 15 eV (27). To improve the signal-to-noise ratio, we averaged 5 images recorded with an exposure time of 1 min each. Phosphorus maps were calculated based on the ratio between the averaged pre- and postedge images (Digital Micrograph; Gatan). To estimate the P content of individual DMV cores, the averaged P signal of 25 ribosomes was used for calibration. After correction for background intensities, measurements were correlated to 7,128 P atoms in a mammalian ribosome (4). This signal was then compared to the P signal in DMV cores, which was also corrected for background noise. While performing these measurements, only cores surrounded by a clear halo, which were likely to be complete and to reside in the middle of the section, were included.

To facilitate the image alignment required for ESI tomogram production, 10-nm gold particles were layered on top of the 75-nm sections as fiducial markers. For ESI tomography, a pre-edge and a post-edge single-axis tilt series were recorded with a Tecnai 12 BioTwin transmission electron microscope operating at 200 kV, using EFTEM tomography software (Gatan). A total of 64 images were recorded at 2° increments between tilt angles of −63° to +63°. For each tilt angle, 5 images were acquired with a cooled slow-scan charge-coupled-device (CCD) camera (2k GIF; Gatan) in 2-by-2 binned mode and averaged to obtain a better signal-to-noise ratio. The electron microscope magnification was ×19,000, corresponding to a pixel size of 2.7 nm at the specimen level. For ESI tomogram computation, the pre-edge tilt series was aligned using the fiducial markers and the IMOD software package (26). These alignments were then transferred to jump ratio tilt series, where the gold markers are not visible, and a reconstruction was computed using 25 iterations of the simultaneous iterative reconstruction technique (SIRT) algorithm implemented in IMOD (17). The 3-D surface-rendered reconstructions of virus-induced structures and adjacent cellular features were processed by surface rendering and thresholding using the AMIRA Visualization Package (TSG Europe).

RESULTS

Time course analysis reveals minimal colocalization between the EAV replicase and accumulating dsRNA. To investigate the accumulation of viral replicase and dsRNA and to establish the most relevant time points for ultrastructural studies, we first studied EAV-infected Vero E6 cells using confocal immunofluorescence microscopy. In particular, we included an anti-dsRNA monoclonal antibody, an antiserum recognizing the nsp3 transmembrane protein, and a new rabbit antiserum recognizing the EAV RdRp nsp9 (61), a core subunit of the viral RTC. Cells were fixed at various time points after infection and immunolabeled (Fig. 1) to establish the time point at which the first signal appeared, its subcellular distribution, and the extent of colocalization of the different arterivirus markers used. Mock-infected control cells were used to confirm the high specificity of each of the three antibodies (Fig. 1A to C, left).

The first labeling of foci for nsp3, nsp9, or dsRNA could be detected in the perinuclear areas of infected cells by 3 h p.i. (data not shown), and by 4 h p.i., most cells were positive (Fig. 1A to C). Using cells fixed every hour from 0 to 15 h p.i., we measured labeling intensities and calculated averages per time point (Fig. 1D). The 4-h p.i. time point was found to mark the start of a rapid increase in the amounts of both dsRNA and EAV replicase (Fig. 1D). Both signals reached a plateau around 9 h p.i. and then slowly declined during the final phase of infection (maximum titers of viral progeny were reached by 15 h p.i. [data not shown]). Replicase subunits nsp3 and nsp9 accumulated in a dense perinuclear ring, whereas dsRNA labeling remained restricted to the same distinct foci observed at 4 h p.i. Compared to the latter time point, the number of dsRNA-positive foci had increased by 7 and 10 h p.i., although the labeling intensities of the individual foci were quite comparable (Fig. 1A and B, insets). The most striking observation was the fact that the colocalization of viral RdRp and dsRNA was very limited (Fig. 1B), even during the early phase of infection, a finding resembling the previously observed separation between the bulk of viral replicase and dsRNA in SARS-CoV-infected cells (23). The colocalization of nsps and dsRNA was quantified at three different time points by calculating the Manders overlap coefficient (Fig. 1E) (28, 33) for each double labeling. By definition, its value ranges from 0 (full separation) to 1 (complete colocalization), and values above 0.5 are generally taken to signify a meaningful level of colocalization. Whereas overlap measurements for dsRNA and replicase, in particular nsp9, exceeded this threshold by 4 h p.i., values at later time points were around or even below 0.5. On the other hand, from the earliest moment of detection on, the labeling patterns for nsp3 and nsp9 approached complete colocalization (Fig. 1E).

Our analysis established that in terms of viral replicase and dsRNA accumulation, and therefore likely also for the formation of viral replication structures, the most relevant window for a detailed analysis is from 4 to 10 h p.i. Moreover, our data suggested an intriguing separation of the sites at which EAV replicase and dsRNA accumulate. This is obvious late in infection, following abundant nsp synthesis from the rapidly accumulating genomic RNA, but essentially also applies at 4 h p.i. At that time point, both markers localized close to each other,
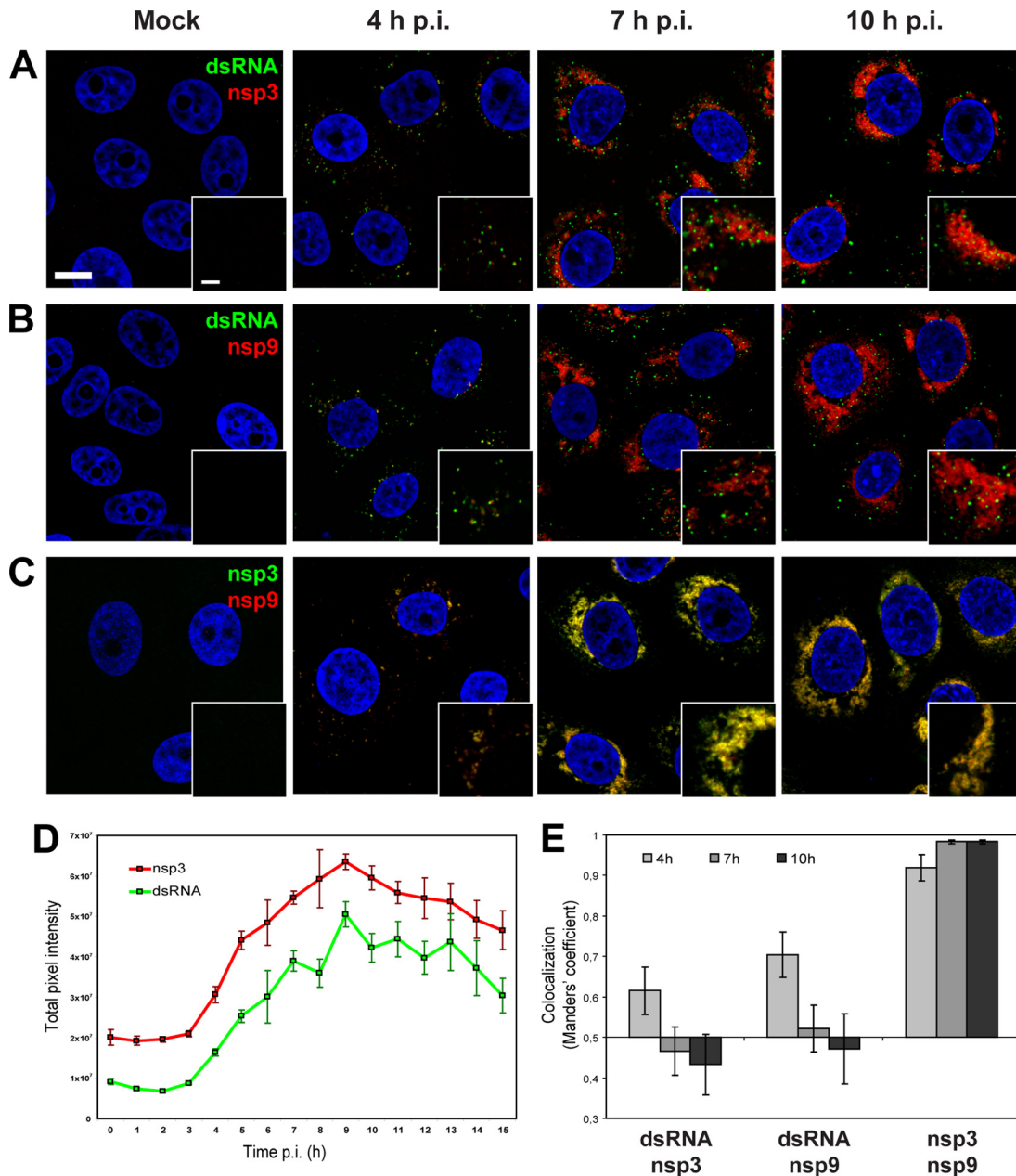
FIG 1 Immunofluorescence analysis of EAV-infected cells. EAV-infected Vero E6 cells were fixed at various time points after infection and processed for IF assays using rabbit antisera recognizing different replicase subunits and a mouse monoclonal antibody specific for dsRNA. Imaging was done using a confocal laser scanning microscope, and quantification of labeling intensity was carried out using wide-field fluorescence microscopy images. Scale bars, 10 μm and 2.5 μm (insets). (A to C) Time course dual-labeling IF assays for dsRNA/nsp3 (A), dsRNA/nsp9 (B), and nsp3/nsp9 (C). At 4 h p.i., the early signals for dsRNA and both nsps were found in close proximity to each other and partially overlapping. At later time points (shown here at 7 and 10 h p.i.), colocalization of dsRNA and either nsp was much less obvious, whereas the signals of nsp3 and nsp9 were still almost completely colocalized. (D) Graph showing the total pixel intensities from images acquired from EAV-infected cells that were fixed every hour between 0 and 15 h p.i. The nsp3 and dsRNA signals were quantified from 5 low-magnification images taken with a 40× objective, each containing about 75 cells. For both nsp3 and dsRNA, the intensity of the signals started to increase exponentially between 3 and 4 h p.i. and peaked at 9 h p.i. The error bars indicate standard deviations. (E) Graph showing the averaged Manders overlap coefficients for dsRNA, nsp3, and nsp9 at 4, 7, and 10 h p.i. ($n = 25$ cells per condition). By definition, Manders overlap coefficients range from 0 to 1, representing full separation and complete colocalization of signals, respectively. We interpreted values above 0.5 as indicative of a certain level of colocalization and values below 0.5 as indicative of a lack of colocalization.

but only a limited number of double-positive foci could be discerned (Fig. 1A and B).

High-pressure cryofixation reveals a compact core structure in EAV DMVs. Previous EM studies of chemically fixed EAV-infected cells identified paired membranes and DMVs with a (largely) electron-lucent interior as the most prominent virus-induced membrane structures and the ER as the most likely platform for their generation (41, 51). During our recent character-
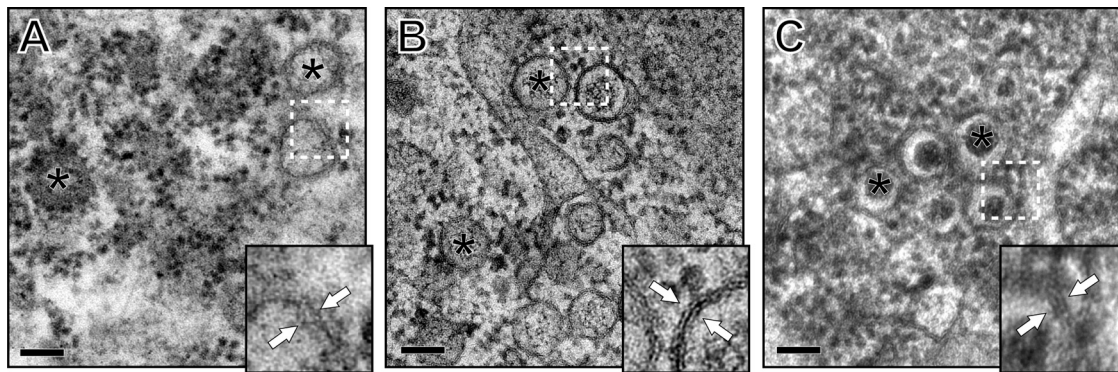
FIG 2 Comparison of DMV morphology after different fixation procedures. EAV-infected Vero E6 cells were fixed at 7 h p.i. using different fixation methods to assess the most suitable preservation protocol for the EAV-induced membrane structures. The asterisks indicate the interiors of DMVs, and the insets are enlargements of the boxed areas, with white arrows pointing to the two bilayers of the DMVs. Scale bars, 100 nm. (A) Chemical fixation with 1.5% glutaraldehyde and, subsequently, 1% osmium tetroxide in 0.1 M sodium cacodylate buffer. The contrast of DMV membranes is relatively poor, and the double membranes are difficult to discern. The DMV interior shows an undefined appearance. (B) Cryofixation by plunge freezing, followed by FS. The lipid bilayers of DMVs are recognizable, and the DMV interior has a more granular appearance. As a result of ice crystal formation, the cytosol surrounding the DMV cluster contained electron-lucent areas. (C) Cryo-fixation by HPF, followed by FS. Overall, membrane contrast was high, and the cytosol was free of freezing artifacts. The interiors of DMVs prepared by HPF were visualized as electron-dense cores that were surrounded by electron-lucent halos.

ization of SARS-CoV-induced replication structures (23, 24, 49), we experienced the fact that virus-induced replication structures can be extremely fragile and that the optimal preservation of their membranes may be a technical challenge. In the case of SARS-CoV samples, biosafety considerations dictated a paraformaldehyde-based prefixation prior to CF and FS. EAV-infected cells could be subjected to CF methods directly (i.e., without prefixation), which is generally believed to minimize fixation artifacts. Therefore, we explored and compared three different fixation techniques to deduce a suitable preservation protocol for EAV replication structures: chemical fixation with glutaraldehyde, CF by plunge freezing, and HPF. As described in Materials and Methods, all samples were stained, dehydrated, and embedded in an epoxy resin, and 100-nm-thick sections were used for EM analysis at 80 kV.

In 7-h p.i. samples, all fixation protocols revealed the presence of typical EAV DMVs (Fig. 2A to C), which were not found in mock-infected cells. Although the tightly apposed double membranes could be recognized in each of the three specimens, membrane contrast was clearly superior in cryofixed cells, facilitating the straightforward visualization of both bilayers (Fig. 2B and C, insets). Chemical fixation suggested that the DMV interior consists of a web of undefined filaments (Fig. 2A), whereas DMVs in plunge frozen samples had a more granular interior (Fig. 2B), similar to what was previously observed for SARS-CoV DMVs (49). Although plunge freezing is generally considered to be an adequate CF procedure, samples are prone to local freeze damage due to ice crystal formation. High-pressure freezing, i.e., limiting ice crystal expansion by pressurizing samples to ~2 × 10^8 Pa prior to freezing, is believed to minimize this problem (45, 55). When using an HPF protocol, we indeed noticed that the overall ultrastructural preservation of EAV-infected cells was significantly improved compared to plunge frozen samples, resulting in a denser cytoplasm due to the lack of segregation artifacts (compare Fig. 2B and C). In the plunge frozen samples, membrane contrast may be more appealing to the untrained eye, due to the more "empty" appearance of the surrounding intracellular space, but this effect is probably caused by the ice crystal-driven deformation of the cytosol. Interestingly, only in HPF samples was the DMV interior

visualized as an electron-dense, roughly spherical mass, which was separated from the inner DMV membrane by an electron-lucent "halo." This compact core structure (diameter, 30 to 100 nm) (Fig. 2C) was never observed in cells that had been either chemically fixed or plunge frozen (Fig. 2A and B).

In summary, the overall morphology of both cellular organelles and EAV replication structures appeared to be improved by the use of CF. Each of the three fixation methods tested could visualize the double membranes of the EAV-induced structures, but the ultrastructural details of the DMV core were different for each technique. We cannot formally exclude the possibility that the striking electron-dense DMV cores revealed upon HPF (Fig. 2C) are an artifact. However, the general consensus that HPF is the most advanced EM preservation technique and our own ultrastructural comparisons (Fig. 2) provided a clear basis for using the HPF protocol as the foundation for our subsequent EM experiments. Still, all of the major findings described below were independently confirmed using plunge frozen samples, and data from this comparison are included to further support some of our key observations regarding membrane connections (Fig. 3H to K; see Video S2 in the supplemental material).

EAV replicates in association with a reticulovesicular network of modified endoplasmic reticulum. Previously, in conventional transmission EM studies, the outer membrane of EAV DMVs was occasionally found to be continuous with ER membranes (41, 51). Because these connections were only rarely observed, this morphology was postulated to represent an intermediate stage of DMV formation, after which outer membrane fission would occur to release a separate vesicular structure that is bound by a double membrane (41). For coronaviruses, using ET-based 3-D reconstruction, we could recently show that DMV outer membranes are connected with each other and with the ER. Accordingly, coronavirus DMVs were concluded to be integrated into a reticulovesicular network that also includes convoluted membranes (23). ET was then applied to EAV-infected cells (Fig. 3) to evaluate the presence of a similar network of structures.
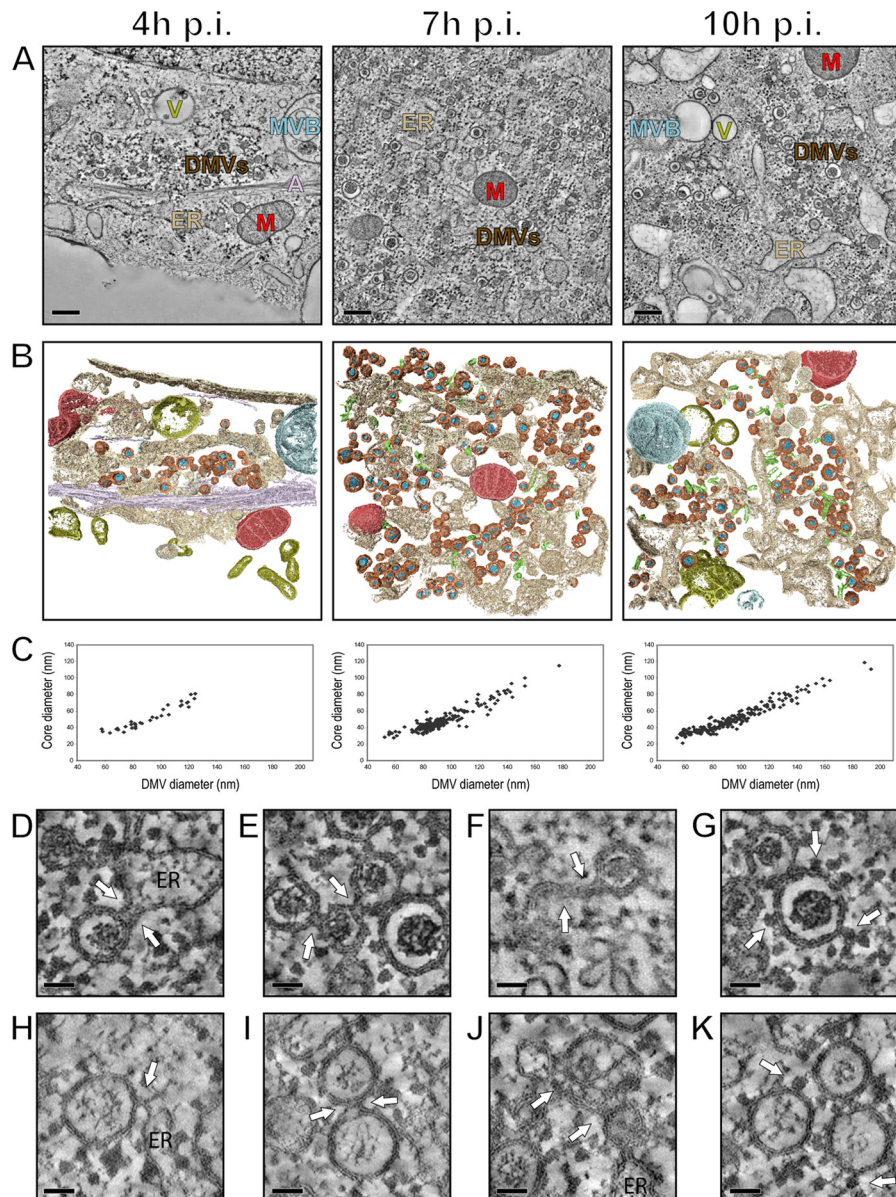
FIG 3 Electron tomography of cytoplasmic areas containing EAV-induced DMVs. (A) EAV-infected Vero E6 cells were high-pressure frozen at 4, 7, and 10 h p.i. and processed for dual-axis electron tomography to obtain 3-D reconstructions of relevant cytoplasmic areas. The images show a 10-nm slice through the tomographic reconstruction of 200-nm-thick resin-embedded sections. Along with DMVs (brown), cores (blue), ER (beige), EAV tubules (green), mitochondria (M; red), smooth-walled vesicles (V; yellow), multivesicular body (MVB; blue-gray), and actin filaments (A; purple) are depicted. Scale bars, 500 nm. (B) 3-D surface-rendered models of the tomograms that were derived from panel A. The models illustrate the relative abundances of DMVs at different time points, the clustering of DMVs, and the cytoplasmic content near the vesicles. The same coloring scheme as in panel A was used to show the different organelles. (C) All DMVs within the tomograms, acquired at 4 ($n = 34$), 7 ($n = 193$), and 10 h p.i. ($n = 194$) and shown in panel B, were delimited *in silico*, counted, and measured in the x and y directions to derive average diameters of the complete DMV and the DMV core. If the equator of an individual DMV was present within the tomogram volume, a subvolume of 250 (x) by 250 (y) by 10 (z) pixels was extracted from the central part of the DMV and merged into a single image representing a 12-nm-thick section through the middle of the DMV. The graph shows the correlation between the average (x, y) diameter of individual DMVs (x axis) and the corresponding average (x, y) diameter of the DMV cores (y axis). (D to G) Close-ups of the tomograms shown in panel A. The arrows indicate connections of DMV outer membranes with the ER (D), other DMVs (E), and curved double-membrane structures (F). Ribosomes were found to decorate the surface of the outer DMV membrane (G, arrows). (H to K) Close-ups of structures comparable to those in panels D to G but derived from plunge frozen samples exhibiting alternative staining and contrast of membrane structures. Scale bars, 50 nm.

EAV-infected Vero E6 cells were high-pressure frozen at 4, 7, and 10 h p.i., and samples were freeze substituted and embedded in an epoxy resin. Serial 200-nm-thick sections were cut to analyze the EAV replication structures in successive sections cut from the same cell. This approach was particularly useful when searching for replication structures in early samples (4 h p.i.), when only small DMV clusters were present (Fig. 3A). This technique also allowed us to produce tomograms from the same relative position, i.e., the center of the region containing replication compartments, in samples fixed at different time points after infection. At 4 h p.i.,

clusters of DMVs were distributed throughout the cytoplasm (Fig. 3B, brown). They were often observed in close proximity to ER cisternae (Fig. 3B, beige) and occasionally near bundles of actin filaments (Fig. 3B, purple). By 7 h p.i., the number of vesicles per cluster had dramatically increased (Fig. 3A and B), and the dimensions of the region containing replication compartments extended beyond the volume of our tomograms (2.5 by 2.5 by 0.2 μm). Nevertheless, our data offered a unique 3-D view of the central space in which EAV replication structures accumulate.

By 7 h p.i., in addition to the developing virus-induced membrane compartments, unusual tubular structures (Fig. 3A and B, green; see Video S1 in the supplemental material) were observed in their immediate vicinity. These tubules were described previously in arterivirus-infected cells (13, 56, 63) and were proposed to be induced by virus infection. Specifically, their formation was found to be linked to the expression of the viral nucleocapsid (N) protein (66), which rapidly increases from 7 h p.i. on. Since it was previously established that the arterivirus N protein is not required for viral RNA synthesis (37), we discuss these tubules separately below (see Fig. 5). By 10 h p.i., the ER of EAV-infected Vero E6 cells had become dilated, which appeared to promote the dispersal of both DMVs and tubules (Fig. 3A and B).

A detailed analysis of membrane structures in both HPF-derived and plunge frozen samples revealed important differences from, as well as striking similarities to, coronavirus replication structures. For DMVs that were entirely or largely included in the volume of our tomograms, we measured the maximum diameters. Throughout the infection, both the average DMV diameter (92 ± 21, 94 ± 20, and 94 ± 27 nm in HPF samples fixed at 4, 7, and 10 h p.i., respectively) and the DMV size distribution were essentially constant. These average diameters are about 3 times smaller than those of SARS-CoV-induced DMVs (300 nm) (23), implying that the average volume of EAV DMVs is about 27 times smaller. The average diameter of EAV DMV cores did not differ significantly between the time points analyzed (52 ± 14, 49 ± 14, and 51 ± 18 nm in HPF samples fixed at 4, 7, and 10 h p.i., respectively). The diameters of the DMV core and the entire DMV appeared to be directly correlated (Fig. 3C), although larger DMVs contained a larger electron-lucent "halo-like" space between the DMV inner membrane and electron-dense core. In all DMVs, at least one side of the core structure touched the inner membrane, although fibrillar structures crossing to the other side of the DMV's inner vesicle were also seen.

The outer membranes of EAV DMVs (n = 500) were found to be continuous with rough ER membranes (Fig. 3D and H) (34%), each other (Fig. 3E and I) (14%), or paired membrane structures (Fig. 3F and J; see Video S1 in the supplemental material) (6%) or were found to have a combination of the above connections (46%). These connections were sometimes hard to visualize in HPF samples, due to the lower membrane contrast, but they were readily observed when ET was applied to plunge frozen EAV-infected Vero E6 cells (Fig. 3H to K; see Video S2 in the supplemental material). Typically, these connections consist of tightly apposed membranes, similar to those previously described for coronaviruses (23, 59). However, the large CM clusters found in coronavirus-infected cells were not observed in the case of EAV infection. The presence of ribosomes on the cytosolic face of EAV DMVs (Fig. 3G and K, arrows) strongly suggested that their outer membranes are indeed derived from the rough ER. Occasionally, both cytosolic surfaces of curved double-membrane sheets (similar to those shown in Fig. 3F) were found to be decorated with ribosomes (data not shown).

As outlined in the introduction, several +RNA virus replication structures have been characterized as spherular membrane invaginations whose interiors are connected to the cytosol. On the other hand, in spite of an extensive ET analysis, such connections could not be identified in the case of the SARS-CoV-induced DMVs (23). We therefore scrutinized EAV-induced DMVs (n = 888, from five different tomograms of HPF samples representing four different time points after infection) for the presence of membrane discontinuities (diameter > 4 nm) that might constitute a connection to the cytosol. For at least 91% of these vesicles, both membranes appeared to be fully intact, and only some of the larger vesicles showed membrane discontinuities that could be interpreted as connections to the cytosol (Fig. 3). Nevertheless, similar openings were also occasionally detected in the membranes of host cell organelles like the ER, suggesting that they are more likely explained by technical issues, such as membrane fragility, freeze damage, and/or staining artifacts. Our results thus suggest that EAV-induced DMVs are closed compartments or at least lack the connections to the cytosol with a diameter on the order of 10 nm that were observed for the replication compartments of various other groups of +RNA viruses (25, 65).

The interiors of EAV DMVs label strongly for double-stranded RNA. Subsequently, IEM was used to confirm the association of the viral replication machinery with the network of EAV-induced double-membrane structures described above. Previously, DMV membranes and the surrounding membrane structures were found to modestly label for nsp2 and nsp3 (41), the two membrane proteins that suffice to induce double-membrane structures (51). In specimens prepared according to our new FS protocol, DMV membranes again labeled for nsp3, and the membranous structures in their vicinity, most likely part of the RVN, also contained immunogold label (Fig. 4A). A similar pattern was obtained using an antiserum recognizing the nsp9 RdRp (Fig. 4B) and the nsp11 endoribonuclease (data not shown), indicating that both membrane-modifying and enzymatic subunits of the EAV replicase are associated with the virus-induced membrane network but are rarely detected in the interior of DMVs.

To also analyze the RNA component of the viral replication process, we next labeled the sections for dsRNA. As in the case of SARS-CoV-infected cells (23), the dsRNA labeling in EAV-infected cells was almost exclusively associated with the interior of the DMVs (Fig. 4C and D [black arrows]; see Fig. S1C in the supplemental material). At first glance, some of the label appeared to localize outside DMV cores (Fig. 4C and D, white arrows), but in these cases, ET analysis of serial sections revealed an association with the contents of "obscured DMVs" that had been cut tangentially and, for the most part, resided in an adjacent section (data not shown).

A quantitative analysis of the immunolabeling data was performed to confirm the specific association of the labeling for dsRNA, as well as nsp3 and nsp9, with the RVN-containing areas of the cell. Using 7-h p.i. samples, overlapping high-magnification images containing at least three whole cells were acquired and merged into a single mosaic image (Fig. 4E). At low magnification, and therefore unbiased with respect to the immunogold labeling, specific areas of the cells were selected and marked by drawing a circle with a diameter of 3.57 μm, thus representing a 10-μm^2 surface area, around them (Fig. 4E). Fifteen such circles were
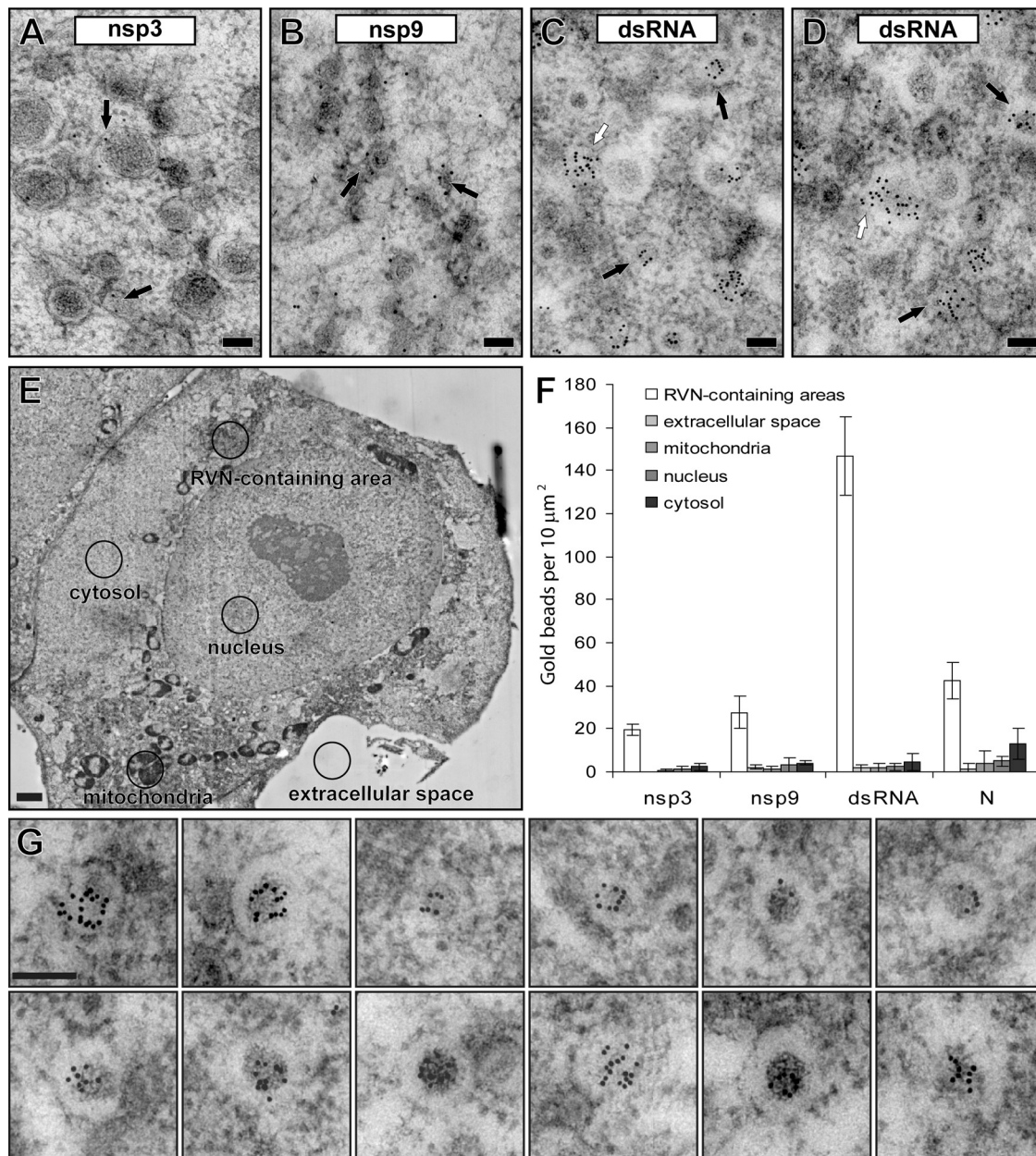
FIG 4 Immunogold labeling of EAV replicase and dsRNA in infected cells. EAV-infected Vero E6 cells (7 h p.i.) were high-pressure frozen and processed for FS and IEM (see Materials and Methods). In all labelings, 10-nm colloidal gold particles conjugated to protein A were used for detection of the primary antibodies. Scale bars, 100 nm. (A and B) Immunolabeling with antisera recognizing different EAV nsp3 (transmembrane protein) and nsp9 (the EAV RdRp) proteins. Label was predominantly found on DMV membranes and their surroundings. (C and D) Immunolabeling for dsRNA, showing extensive clustering of label on DMV cores (black arrows). Some clusters of label seemed to be localized outside DMVs (white arrows); however, electron tomography combined with serial sectioning indicated the presence of obscured DMV "caps" as a result of sectioning. (E) Example of a low-magnification mosaic image of a whole cell (from a section immunolabeled for dsRNA) and the marking of the five different compartments that were used for a quantitative analysis of the immunolabeling. Scale bar, 2.5 μm. (F) The specific association with RVN-containing areas in EAV-infected cells (at 7 h p.i.), or lack thereof, was verified for the immunogold-labeling experiments using antibodies recognizing nsp3, nsp9, dsRNA, and N protein (Fig. 5B). For each labeling, the gold beads inside different cellular compartments (*n* = 3) (see panel E and main text) were counted, and means and standard deviations are shown. (G) Gallery of close-ups of EAV-induced DMVs highlighting the highly specific association of the labeling for dsRNA with the DMV core structure.

placed in mosaic images of at least three different cells to mark the extracellular space, nucleus, cytosol, mitochondrion-containing areas, and RVN-containing areas. The last were defined as perinuclear areas with high electron density that did not contain mitochondria. Subsequently, the presence of DMVs in these RVN-

containing areas was confirmed at high magnification, and the gold beads inside each area were counted (Fig. 4F). This analysis confirmed that the labeling for nsp3, nps9, and dsRNA was specifically associated with the RVN/DMV-containing areas and essentially absent from the cytosol, nucleus, extracellular space, and

mitochondrion-containing regions. The high-magnification images of the RVN-containing areas further confirmed the specific association of the dsRNA labeling with the DMV core structure (Fig. 4G). Taken together, our analysis clearly established that the cores of EAV-induced DMVs labeled abundantly for dsRNA but were essentially devoid of labeling for different replicase subunits.

EAV-induced cytosolic tubules contain the viral nucleocapsid protein. In our tomograms of EAV-infected cells fixed at 7 h p.i. or later (Fig. 3), we observed tubular structures in close proximity to DMVs. As discussed above, previous arterivirus studies suggested that these tubules contain the viral N protein. In particular, Wieringa and coworkers described the absence of tubule formation in cells transfected with RNA of an EAV mutant lacking a functional N protein gene (66). Nonetheless, EAV N protein overexpression, in the absence of infection, did not induce similar tubules, suggesting a requirement for additional infection-related factors.

To further analyze the origin and ultrastructure of these EAV-induced tubules, immunofluorescence microscopy was used to establish that N protein expression and tubule formation indeed coincide. Vero E6 cells fixed at various time points after infection were double labeled for nsp3 and N and analyzed by laser scanning confocal microscopy (Fig. 5A). At 4 h p.i., nsp3 signal was visible in most of the infected cells; however, N protein was not yet detectable in any of them (Fig. 5A). At 7 h p.i., the N protein labeling intensities varied between cells, probably reflecting a certain asynchronicity of infection. As documented previously (37), in cells still containing little N protein, the signal overlapped with nsp3, a marker for the replication structures (Fig. 5A, close-ups I and II, arrows). Cells in which infection was more advanced (Fig. 5A) also showed N protein accumulation in the rest of the cytoplasm, where the protein may be present in soluble form or as part of newly assembled virions.

With our IEM protocols, the EAV-induced tubules were clearly visible, and immunogold labeling showed that the tubules contained N protein (Fig. 5B, black arrows), whereas a small fraction was found in close association with DMV membranes (Fig. 5B, white arrows). Quantification of the immunolabeling (Fig. 4E and F) primarily showed the specific association of the labeling with the RVN-containing regions. Furthermore, as expected, some of the labeling was found in the cytosol.

Next, we analyzed the tubules in 8-h p.i. tomograms and found that they are actually sheets that locally branched into tubules with an average diameter of 42.8 ± 4.6 nm ($n = 50$) (Fig. 5C and D, arrows; see Video S1 in the supplemental material). Compared to the clearly visible DMV and host cell membranes, the morphology of the tubules was different and always showed a single electron-dense layer rather than the well-known bilayer profile of a lipid membrane (Fig. 5E). This strongly suggested that these structures, which are closely associated with the EAV-induced RVN but lack clear connections (Fig. 5F; see Video S1 in the supplemental material), constitute protein sheets rather than membranes.

Visualization and quantification of the RNA content of DMV cores by electron spectroscopic imaging. Few quantitative data are available on the RNA and protein contents of +RNA virus replication structures (25, 43, 48, 65). Using replicon cell lines and a combination of biochemical techniques, Quinkert et al. (43) concluded that hepatitis C virus establishes about 100 replication complexes per cell, requiring (at best) only a few percent of the available nonstructural proteins. For FHV replication structures,

Kopek and coworkers (25) quantified the RNA and protein contents biochemically and related these measurements to the number of spherules per cell (estimated to be 20,000 ± 11,000). They derived an overall estimate of the RTC composition, but these biochemical approaches do not allow the analysis of individual replication structures. In a first attempt to address this issue, we applied the EM-based method of electron spectroscopic imaging (ESI) to the EAV-induced DMVs. This EM technique is based on imaging only with inelastically scattered electrons that suffer a specific energy loss as a result of collisions with electrons in the specimen (27). The magnitude of this energy loss is element specific and can be used to derive a so-called elemental map that reveals the concentration of a given element in the specimen. Recently, ESI has been successfully applied to biological samples, for example, to visualize the distribution of nucleic acids and proteins within the cell's nucleus based on the signals for phosphorus and nitrogen, respectively (1, 2, 12).

Based on our dsRNA labeling (Fig. 4C and D), we expected DMV cores to contain large amounts of RNA and thus phosphorus (P), an element with relatively low abundance in the protein component of ribonucleoprotein complexes (12). Thus, we explored whether ESI could be used to visualize DMV cores and assess their RNA content on the basis of the P signal by using a 200-kV EM equipped with a postcolumn energy filter. EAV-infected cells were high-pressure frozen at 8 h p.i., freeze-substituted in acetone containing 1% glutaraldehyde, and cut into 60-nm-thick sections. Contrasting agents were omitted to prevent background signal in our elemental maps. As a consequence, the contrast of the sample was very low, but DMVs were easily recognized by their cores, which were clearly visible in images collected in zero-loss mode (with only electrons not encountering any collisions) (Fig. 6A, asterisks). Next, P maps were acquired by calculating the ratio between the pre-edge (Fig. 6B) and post-edge (Fig. 6C) images, which reflect the electrons that encountered background scattering and phosphorus-specific scattering, respectively (see Materials and Methods for more details). In these P maps, DMV cores were easily distinguishable (Fig. 6D and E, asterisks) and were found to indeed contain a large amount of P. Surprisingly, the characteristic N protein-containing tubules also showed up in the P maps (Fig. 6D and E, arrows).

Since the average EAV DMV core diameter of about 50 nm was close to the thickness of our sections (60 nm), most cores were not entirely included in our sections and spherical caps of various sizes were missing. Therefore, to estimate the RNA contents of individual DMV cores, we measured the P signals of those cores that contained a clear electron-lucent halo and thus contained most or all of the original core volume (the cores marked with asterisks in Fig. 6D and E). Ribosomes, which were clearly visible in the cytosol (Fig. 6G, circles), were used to calibrate the P measurements on the basis of their known RNA contents (2, 12). After correction for background signal, the P measurements of 11 DMV cores were compared to the averaged P signal measured for 25 ribosomes, each containing 7,128 nucleotides of rRNA (4). Our calculations indicated that these 11 cores contained 0.9×10^5 to 3.5×10^5 P atoms, with an average of 1.7×10^5, the equivalent of about 13 EAV genomes. In order to visualize the P distribution within the DMV cores, we acquired electron spectroscopic tomograms to derive 3-D P maps (Fig. 6F to H; see Video S3 in the supplemental material) (2). This revealed thread-like structures that did not appear to extend into the cytosol (Fig. 6G and H). The ESI ET
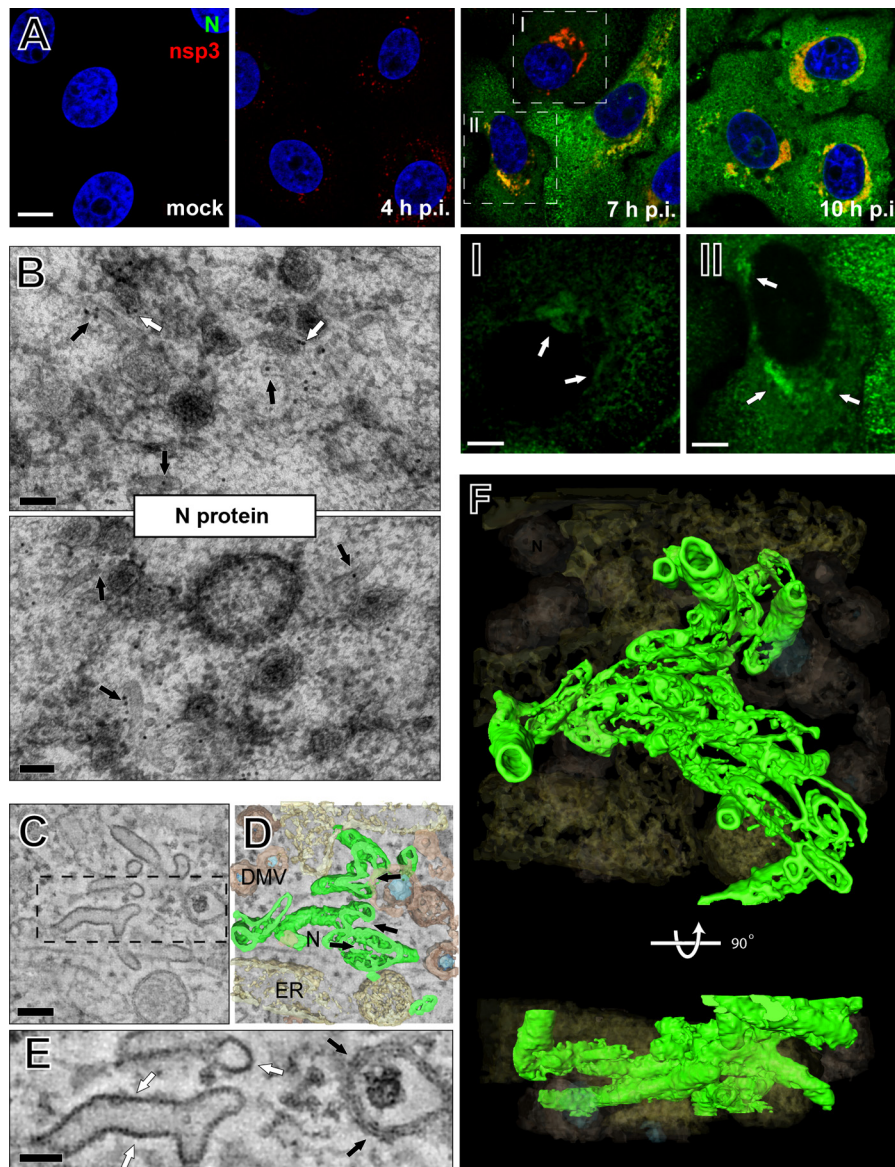
FIG 5 Nucleocapsid protein-containing structures are intertwined with EAV-induced replication structures. (A) EAV-infected Vero E6 cells were fixed at various time points after infection, processed for IF microscopy using dual labeling for nsp3 and N protein, and analyzed by confocal laser scanning microscopy. By 4 h p.i., nsp3 signal was visible in most of the infected cells, but N protein was not yet detectable. Although the intensity varied between cells, N protein signal became detectable in most cells by 7 h p.i. and partially overlapped with nsp3 signal (close-ups I and II, white arrows). By 10 h p.i., N protein had become distributed throughout the cytoplasm of infected cells. Scale bars, 10 μm (A) and 5 μm (close-ups). (B) EAV-infected Vero E6 cells were high-pressure frozen at 8 h p.i., processed for FS, and immunogold labeled for the N protein. The majority of the label was found to be associated with EAV-induced tubular structures (black arrows) and DMVs (white arrows). Scale bars, 100 nm. (C) EAV-infected Vero E6 cells were high-pressure frozen at 8 h p.i. and processed for dual-axis electron tomography (see also Fig. 3). This 5-nm-thick slice illustrates the relatively high electron density of the EAV-induced tubules. Scale bar, 100 nm. (D) Three-dimensional ET reconstruction illustrating the local openings in tubules (N, depicted in green) and proximity of DMVs (depicted in brown, with cores in blue) and the ER (beige). (E) Close-up of panel C (boxed area) illustrating the morphological difference between the dense single layer constituting the tubules (white arrows) and the double bilayer of DMV membranes (black arrows). The arrows indicate areas where the tubules or membranes run in parallel with the electron beam and thus contain the maximum resolution in *x* and *y*. Scale bar, 50 nm. (F) 3-D ET reconstruction illustrating the distribution and architecture of the EAV tubules (depicted in green) and their proximity to the DMVs (depicted in brown, with cores in blue and the ER in beige).

analysis revealed that, compared to DMV cores, the density of the P signal was higher in ribosomes (Fig. 6F), suggesting that ribosomal RNAs are packed more densely than the RNA within the EAV-induced DMVs. Clearly, a more extensive structural characterization of DMV cores is required, including ESI experiments targeting their protein content, but in any case, the first application of ESI to virus-infected cells established the potential of this novel tool to investigate both the structure and the composition of cytoplasmic viral replication structures.

DISCUSSION

Reshaping the endoplasmic reticulum to accommodate arterivirus RNA synthesis. The in-depth dissection of ultrastructural changes in infected cells is an important starting point for under-
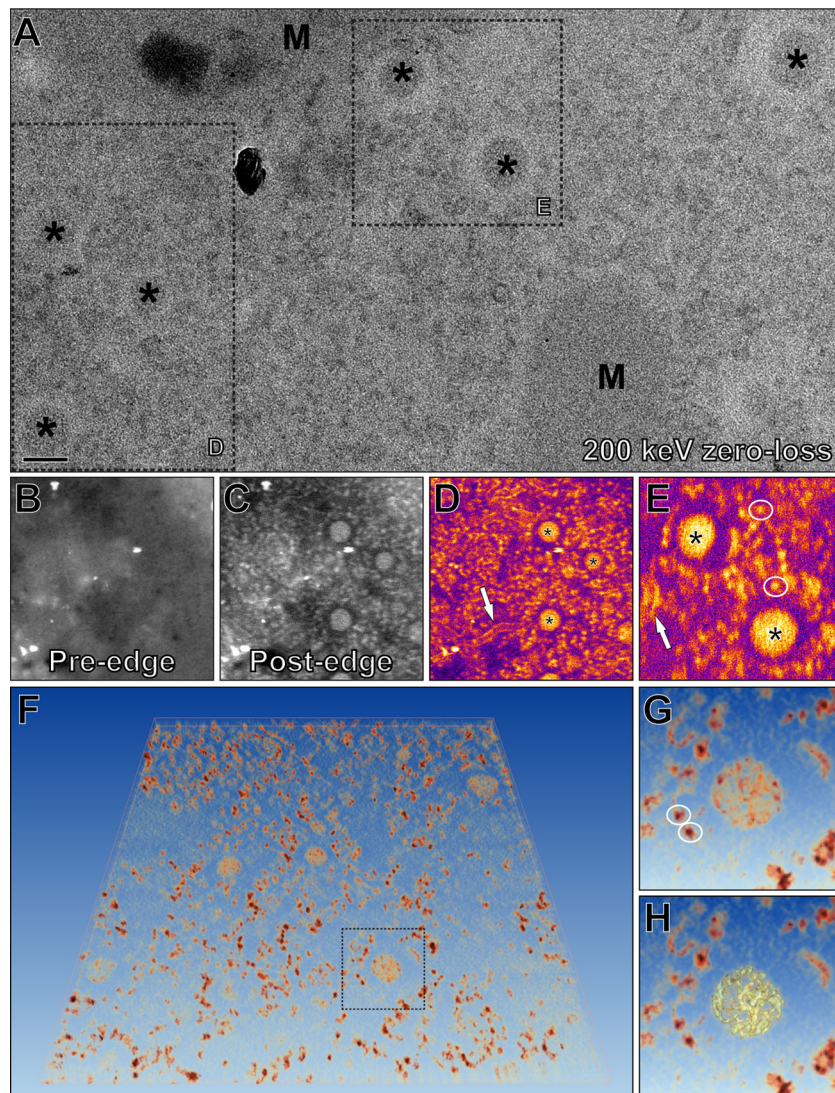
FIG 6 Visualization of RNA inside EAV-induced DMVs by electron spectroscopy imaging-based phosphorus mapping. EAV-infected cells (8 h p.i.) were high-pressure frozen, freeze substituted, and cut into 60-nm-thick sections. Scale bar, 100 nm. (A) 200-kV zero-loss image showing part of the EAV-infected cytoplasm containing DMV cores (asterisks) and mitochondria (M). (B and C) Phosphorus elemental maps were obtained by acquisition of pre-edge (B) and post-edge (C) images at 120- and 157-eV electron loss, respectively, with a 15-eV slit width. (D and E) Phosphorus maps were derived from the boxed areas in panel A by calculating the ratio between the pre- and post-edge intensities, which clearly revealed the P contents of DMV cores (asterisks), ribosomes (circled), and EAV N protein-containing tubules (arrows). (F) An ESI tomogram was recorded at the P energy edge, and direct volume rendering was used to visualize the P content in 3-D. The boxed area is enlarged in panels G and H. (G) Besides the abundant ribosomes (circled), the cores of EAV-induced DMVs were clearly visible. (H) DMV core highlighted with an isosurface that was created by thresholding using a gray value that revealed isolated ribosomes. The resulting isosurface suggests a thread-like ultrastructure of the RNA content inside.

standing how +RNA viruses use and modify cellular infrastructure to create an environment that is optimally suited to their genome replication and gene expression. Ultrastructural studies can define a spatial and temporal framework to integrate cell biological and biochemical data from infected systems and thus contribute significantly to our overall understanding of the replicative cycle of +RNA viruses. The analysis of the biogenesis and function of +RNA virus replication structures is critical to assess parallels and differences between virus families and may reveal opportunities to develop novel antiviral strategies.

In the present study, the combination of HPF and ET was used to define the 3-D architecture of an EAV-induced RVN of modi-fied ER, which includes much smaller but again interconnected DMVs with an electron-dense inner core structure (Fig. 2 and 3). Some striking parallels were observed with coronavirus replication structures (23, 59). Despite the ~27-fold-smaller volume, on average, of arterivirus-induced DMVs, important parallels included the general DMV morphology, the presence of ribosomes on DMV outer membranes (Fig. 3D to G), the connectivity of DMV outer membranes with each other and the rough ER (Fig. 3D and E), and their immunolabeling properties, in particular, the abundant presence of signal for dsRNA in the interiors of DMVs induced by both virus groups (Fig. 4). The finding that these structures have neck-like connections with the ER confirms previous

observations during conventional EM studies (41), which were the basis for the hypothesis that these ER-connected DMVs represent an intermediate stage in the formation of fully detached DMVs. However, our present ET data suggest that DMVs are connected with the RVN (Fig. 3D and H; see Video S2 in the supplemental material), a conclusion supported in particular by our ET analysis, in which each DMV outer membrane was found to have at least one connection to another RVN membrane structure. Arteriviruses thus appear to belong to the +RNA virus groups that induce an elaborate network of modified ER membranes, as was also documented for coronaviruses (23), flaviviruses (18, 65), hepatitis C virus (21), and some picornaviruses (6). By 10 h p.i., the ER of EAV-infected Vero E6 cells became dilated, as was also documented for the late stages of SARS-CoV infection in the same cell line (23). The densely concentrated DMV clusters dispersed into smaller clusters that stayed in close proximity to ER membranes and EAV-induced tubules (Fig. 3A and B). The morphology of individual DMVs at 10 h p.i. seemed indistinguishable from those found at earlier time points. Unlike the late stages of SARS-CoV infection, we did not observe the formation of "vesicle packets," dilated outer membrane sacs containing up to a few dozen DMV inner vesicles (23).

As previously reported for picornaviruses (38, 46), the use of HPF can dramatically alter the appearance of viral replication structures, like DMVs. In the case of EAV, the use of HPF had a major impact on the appearance of DMVs (Fig. 2), which were found to contain an electron-dense core that was not observed after conventional chemical fixation or plunge freezing. By IEM, we established that the labeling for dsRNA (Fig. 4C, D, and G) was associated with these cores but that the nsp labeling was predominantly found on the surrounding RVN membranes. Strikingly, CM similar to those previously found to carry large amounts of coronavirus nsps (23, 59) were not observed upon infection with EAV. Clearly, the large evolutionary distance between the two nidovirus subgroups and their respective replicase subunits involved in intracellular membrane modification leaves ample space to explain such differences, e.g., on the basis of the specific characteristics and expression levels of their transmembrane nsps. For EAV, in the absence of virus replication, expression of nsp2 and nsp3 induces the formation of DMV-like structures (42, 51), which appear to lack the typical content observed in DMVs in cryofixed infected cells (data not shown). A similar "surrogate system" to study coronavirus-induced replication structures remains to be developed.

The exact site of nidovirus RNA synthesis in infected cells remains to be pinpointed. In future studies, it will be imperative to differentiate between, on one hand, the abundantly produced replicase proteins, their subcellular localization, and the various membrane structures they appear to induce and, on the other hand, the actual RNA-synthesizing enzyme complexes, whose number may be just as restricted as previously estimated for some other +RNA viruses. Thus, the overall nidovirus nsp localization in the infected cell is unlikely to reflect the position and abundance of active RTCs. Along the same lines, it may be tempting to propose that the abundant labeling of corona- and arterivirus DMV cores for dsRNA reflects the site of active viral RNA synthesis, but this assumption remains to be supported by approaches allowing the *in situ* analysis of viral RNA synthesis in a much shorter time frame than the many hours of infection during which dsRNA signal is allowed to accumulate in most studies. In this context, the technical possibilities of the ESI approach introduced in this study certainly merit further exploration (see below).

Quantitative ET analysis of EAV-induced DMVs during the first phase of infection clearly showed that the number of vesicles increased rapidly, in particular between 4 and 7 h p.i., but that the average DMV and core diameter remained more or less the same throughout infection (Fig. 3C). Thus, DMVs are apparently primed to develop to a relatively uniform size, although at present, the mechanism of inner-vesicle formation remains as obscure as it is for coronaviruses (23). Whereas the interiors of the membrane invaginations induced by noda-, alpha-, and flaviviruses were found to be connected to the cytosol (18, 25, 65), which presumably is important for the import of building blocks and the export of viral RNA products, convincing evidence for such a connection to the cytosol was not obtained when SARS-CoV-induced DMVs were analyzed in detail by ET (23, 24). This finding is difficult to reconcile with the accumulation of dsRNA, the presumed intermediate and marker of viral RNA synthesis, inside these structures and with *in vitro* studies with isolated RTCs, suggesting that viral RNA synthesis occurs within membrane structures (62). Nevertheless, our ET analysis now produced very similar findings for EAV DMVs and could not unambiguously identify connections with the cytosol. If the interiors of the apparently closed DMVs indeed constitute the site of viral RNA synthesis, this raises the question of how RNA is exported to the cytosol for translation and packaging. An alternative model could involve RNA synthesis in a closed DMV compartment followed by disruption of the membrane to release RNA products, although neither cores devoid of membranes nor cytosolic dsRNA labeling was detected in our EM studies. Finally, since direct evidence for RNA synthesis inside arteri- or coronavirus-induced DMVs remains to be obtained, it is important to point out that the induction of these structures by "simple replicase overexpression" or in the context of cellular antiviral responses cannot be excluded at present.

ESI as a novel approach to dissecting +RNA viral replication structures. To our knowledge, our study is the first to use ESI for the analysis of +RNA virus replication structures. Making use of the high P content of RNA compared to proteins, and with lipids being extracted during the FS procedure, the technique was found to provide both ultrastructural and quantitative information about DMV cores. Although our analysis must have underestimated the amount of RNA for some of the cores, the spherical caps of which were lost during the sectioning of our specimens, the 11 DMV cores analyzed were found to have an average P content that is equivalent to about a dozen RNA molecules of the size of the EAV genome (12.7 kb). Future experiments will be aimed at confirming the viral nature of these molecules, which formally remains to be proven. Clearly, ESI will not be able to distinguish positive- from negative-strand RNA, and also, the question of whether nidovirus genome replication and subgenomic RNA synthesis occur in the same complexes remains to be studied in more detail. Most importantly, however, we first need to distinguish between viral RNA synthesis occurring directly in the cores of nidovirus-induced DMVs on one hand and the accumulation of RNA produced elsewhere in the cell on the other hand. For this, metabolic RNA-labeling experiments, using short pulse-labeling with radiolabeled or chemically modified nucleosides (or nucleotide triphosphates), will be required. Also the biochemical characterization of the RVN and its components, either *in situ* or following their isolation from infected cells, should be expanded to

obtain additional information on the composition and function of these virus-induced membrane structures. In addition to the possibilities for RNA quantification by ESI (12), we have now also gained the first structural information about the interior of DMV cores (Fig. 6F to H; see Video S2 in the supplemental material), although it is clearly too early to speculate about its internal organization in any detail. In the future, it will be worthwhile to explore the use of a combination of different elemental maps to analyze and compare the replication structures of different +RNA viruses in considerable detail.

Is there a structural connection between the arterivirus-induced RVN and nucleocapsid assembly? In addition to the ultrastructure of the EAV-induced RVN, our analysis also documented the previously observed N protein-containing structures in unprecedented detail. During the central stage of infection (7 to 10 h p.i.), this network of tubules rapidly expands and becomes intertwined with the components of the RVN (Fig. 3 and 5). Our EM analysis strongly suggests the absence of lipid membranes in these structures and revealed (putative) protein sheets whose local curvature appears to give rise to the tubular structures (Fig. 5C and D). Immunolabeling directly confirmed the presence of N protein in these tubules (Fig. 5B). Interestingly, the electron density of the tubules in our tomograms was significantly higher than the density of structures known to be solely composed of proteins, like microtubules (data not shown). Previous studies by Wieringa and coworkers (66) indicated that tubule formation depends on both infection/replication and the synthesis of the EAV N protein, i.e., N protein expression itself does not induce tubule formation. The fact that the tubules were clearly visible in our ESI P maps could well reflect the presence of RNA. Formally, P signal could also be derived from the reported phosphorylation of the N protein (at an unknown number of residues [10, 67]), but this explanation may be considered less likely, since a hyperphosphorylated protein domain like the C-terminal region of RNA polymerase II remained undetectable in a recent ESI study (12). Arterivirus assembly has not been studied in much detail so far. Budding of preassembled nucleocapsid structures has been reported to occur at smooth intracellular membranes (8, 32, 63). Particularly intriguing EM observations were made by Wada and coworkers (see Fig. 3G and H in reference 63), who documented tubules (average diameter, 42 nm) extending from the cytosol into virions that were in the process of budding. Recent cryo EM studies on the structure of the arterivirus procine reproductive and respiratory syndrome virus (PRRSV) describe the core of that virion as a double-layered hollow structure with an average diameter of 39 nm (53). This diameter is remarkably close to the average tubule diameter for EAV-induced tubules reported by Wada et al. (63) and our own measurements in this study. Clearly these N protein-containing tubules need to be investigated in more detail, but assuming they constitute a complex of viral RNA and N protein, and given their proximity to the RVN, they may represent a key step in arterivirus nucleocapsid formation and thus an important structural intermediate in the pathway from genome synthesis to virion assembly. Also, studies with other +RNA viruses suggest the existence of mechanisms to organize different stages of the replicative cycle, from genome translation to virus assembly, in the intracellular space (3, 30, 65). The in-depth analysis of such "viral factories" (9, 40) is a technically challenging research area, but recent pioneering ultrastructural studies illustrate how technical advances like ET, and now ESI, may provide new insights into the morphogenesis, structure, and function of these structures that are key to +RNA virus replication and evolution.

REFERENCES

1. **Ahmed K, Li R, Bazett-Jones DP.** 2009. Electron spectroscopic imaging of the nuclear landscape. Methods Mol. Biol. **464:**415–423.
2. **Aronova MA, et al.** 2007. Three-dimensional elemental mapping of phosphorus by quantitative electron spectroscopic tomography (QuEST). J. Struct. Biol. **160:**35–48.
3. **Bamunusinghe D, Seo J-K, Rao ALN.** 2011. Subcellular localization and rearrangement of endoplasmic reticulum by brome mosaic virus capsid protein. J. Virol. **85:**2953–2963.
4. **Belin S, et al.** 2010. Purification of ribosomes from human cell lines. Curr. Protoc. Cell Biol. Chapter 3:Unit 3.40.
5. **Bienz K, Egger D, Pasamontes L.** 1987. Association of polioviral proteins of the P2 genomic region with the viral replication complex and virus-induced membrane synthesis as visualized by electron microscopic immunocytochemistry and autoradiography. Virology **160:**220–226.
6. **Bienz K, Egger D, Pfister T, Troxler M.** 1992. Structural and functional characterization of the poliovirus replication complex. J. Virol. **66:**2740–2747.
7. **David-Ferreira JF, Manaker RA.** 1965. An electron microscope study of the development of a mouse hepatitis virus in tissue culture cells. J. Cell Biol. **24:**57–78.
8. **Dea S, Sawyer N, Alain R, Athanasseous R.** 1995. Ultrastructural characteristics and morphogenesis of porcine reproductive and respiratory syndrome virus propagated in the highly permissive MARC-145 cell clone. Adv. Exp. Med. Biol. **380:**95–98.
9. **den Boon JA, Ahlquist P.** 2010. Organelle-like membrane compartmentalization of positive-strand RNA virus replication factories. Annu. Rev. Microbiol. **64:**241–256.
10. **de Vries AAF, Chirnside ED, Horzinek MC, Rottier PJM.** 1992. Structural proteins of equine arteritis virus. J. Virol. **66:**6294–6303.
11. **Doll ER, Bryans JT, McCollum WH, Crowe MEW.** 1957. Isolation of a filterable agent causing arteritis of horses and abortion by mares. Its differentiation from the equine abortion (influenza) virus. Cornell Vet. **47:**3–41.
12. **Eskiw CH, Rapp A, Carter DRF, Cook PR.** 2008. RNA polymerase II activity is located on the surface of protein-rich transcription factories. J. Cell Sci. **121:**1999–2007.
13. **Estes PC, Cheville NF.** 1970. The ultrastructure of vascular lesions in equine viral arteritis. Am. J. Pathol. **58:**235–253.
14. **Fang Y, Snijder EJ.** 2010. The PRRSV replicase: exploring the multifunctionality of an intriguing set of nonstructural proteins. Virus Res. **154:**61–76.
15. **Fontana J, et al.** 2010. Three-dimensional structure of Rubella virus factories. Virology **405:**579–591.
16. **Froshauer S, Kartenbeck J, Helenius A.** 1988. Alphavirus RNA replicase is located on the cytoplasmic surface of endosomes and lysosomes. J. Cell Biol. **107:**2075–2086.
17. **Gilbert P.** 1972. Iterative methods for the three-dimensional reconstruction of an object from projections. J. Theor. Biol. **36:**105–117.
18. **Gillespie LK, Hoenen A, Morgan G, Mackenzie JM.** 2010. The endoplasmic reticulum provides the membrane platform for biogenesis of the flavivirus replication complex. J. Virol. **84:**10438–10447.
19. **Goldsmith CS, et al.** 2004. Ultrastructural characterization of SARS coronavirus. Emerg. Infect. Dis. **10:**320–326.
20. **Gorbalenya AE, Enjuanes L, Ziebuhr J, Snijder EJ.** 2006. Nidovirales: evolving the largest RNA virus genome. Virus Res. **117:**17–37.

21. **Gosert R, et al.** 2003. Identification of the hepatitis C virus RNA replication complex in Huh-7 cells harboring subgenomic replicons. J. Virol. **77**:5487–5492.

22. **Gosert R, Kanjanahaluethai A, Egger D, Bienz K, Baker SC.** 2002. RNA replication of mouse hepatitis virus takes place at double-membrane vesicles. J. Virol. **76**:3697–3708.

23. **Knoops K, et al.** 2008. SARS-coronavirus replication is supported by a reticulovesicular network of modified endoplasmic reticulum. PLoS Biol. **6**:e226.

24. **Knoops K, et al.** 2010. Integrity of the early secretory pathway promotes, but is not required for, severe acute respiratory syndrome coronavirus RNA synthesis and virus-induced remodeling of endoplasmic reticulum membranes. J. Virol. **84**:833–846.

25. **Kopek BG, Perkins G, Miller DJ, Ellisman MH, Ahlquist P.** 2007. Three-dimensional analysis of a viral RNA replication complex reveals a virus-induced mini-organelle. PLoS Biol. **5**:e220.

26. **Kremer JR, Mastronarde DN, McIntosh JR.** 1996. Computer visualization of three-dimensional image data using IMOD. J. Struct. Biol. **116**:71–76.

27. **Leapman RD, Aronova MA.** 2007. Localizing specific elements bound to macromolecules by EFTEM. Methods Cell Biol. **79**:593–613.

28. **Li Q, et al.** 2004. A syntaxin 1, Galpha(o), and N-type calcium channel complex at a presynaptic nerve terminal: analysis by quantitative immunocolocalization. J. Neurosci. **24**:4070–4081.

29. **Limpens RWAL, et al.** 2011. The transformation of enterovirus replication structures: a three-dimensional study of single- and double-membrane compartments. MBio **2**:e00166–11.

30. **Mackenzie J.** 2005. Wrapping things up about virus RNA replication. Traffic **6**:967–977.

31. **MacLachlan NJ, et al.** 1998. Serologic response of horses to the structural proteins of equine arteritis virus. J. Vet. Diagn. Invest. **10**:229–236.

32. **Magnusson P, Hyllseth B, Marusyk H.** 1970. Morphological studies on equine arteritis virus. Arch. Gesamte Virusforsch. **30**:105–112.

33. **Manders EMM, Verbeek FJ, Aten JA.** 1993. Measurement of co-localization of objects in dual color confocal images. J. Microsc. **169**:375–382.

34. **Miller DJ, Schwartz MD, Ahlquist P.** 2001. Flock house virus RNA replicates on outer mitochondrial membranes in Drosophila cells. J. Virol. **75**:11664–11676.

35. **Miller S, Krijnse Locker J.** 2008. Modification of intracellular membrane structures for virus replication. Nat. Rev. Microbiol. **6**:363–374.

36. **Miyanari Y, et al.** 2007. The lipid droplet is an important organelle for hepatitis C virus production. Nat. Cell Biol. **9**:1089–1097.

37. **Molenkamp R, et al.** 2000. The arterivirus replicase is the only viral protein required for genome replication and subgenomic mRNA transcription. J. Gen. Virol. **81**:2491–2496.

38. **Monaghan P, Cook H, Jackson T, Ryan M, Wileman T.** 2004. The ultrastructure of the developing replication site in foot-and-mouth disease virus-infected BHK-38 cells. J. Gen. Virol. **85**:933–946.

39. **Murk JLAN, et al.** 2003. Influence of aldehyde fixation on the morphology of endosomes and lysosomes: quantitative analysis and electron tomography. J. Microsc. **212**:81–90.

40. **Novoa RR, et al.** 2005. Virus factories: associations of cell organelles for viral replication and morphogenesis. Biol. Cell **97**:147–172.

41. **Pedersen KW, van der Meer Y, Roos N, Snijder EJ.** 1999. Open reading frame 1a-encoded subunits of the arterivirus replicase induce endoplasmic reticulum-derived double-membrane vesicles which carry the viral replication complex. J. Virol. **73**:2016–2026.

42. **Posthuma CC, et al.** 2008. Formation of the arterivirus replication/transcription complex: a key role for nonstructural protein 3 in the remodeling of intracellular membranes. J. Virol. **82**:4480–4491.

43. **Quinkert D, Bartenschlager R, Lohmann V.** 2005. Quantitative analysis of the hepatitis C virus replication complex. J. Virol. **79**:13594–13605.

44. **Salonen A, Ahola T, Kaariainen L.** 2005. Viral RNA replication in association with cellular membranes. Curr. Top. Microbiol. Immunol. **285**:139–173.

45. **Sartori N, Richter K, Dubochet J.** 1993. Vitrification depth can be

46. **Schlegel A, Giddings TJ, Ladinsky MS, Kirkegaard K.** 1996. Cellular origin and ultrastructure of membranes induced during poliovirus infection. J. Virol. **70**:6576–6588.

47. **Schonborn J, et al.** 1991. Monoclonal antibodies to double-stranded RNA as probes of RNA structure in crude nucleic acid extracts. Nucleic Acids Res. **19**:2993–3000.

48. **Schwartz M, et al.** 2002. A positive-strand RNA virus replication complex parallels form and function of retrovirus capsids. Mol. Cell **9**:505–514.

49. **Snijder EJ, et al.** 2006. Ultrastructure and origin of membrane vesicles associated with the severe acute respiratory syndrome coronavirus replication complex. J. Virol. **80**:5927–5940.

50. **Snijder EJ, Spaan WJM.** 2006. Arteriviruses, p 1337–1355. *In* Knipe DM, et al (ed), Fields virology. Lippincott, Williams & Wilkins, Philadelphia, PA.

51. **Snijder EJ, van Tol H, Roos N, Pedersen KW.** 2001. Non-structural proteins 2 and 3 interact to modify host cell membranes during the formation of the arterivirus replication complex. J. Gen. Virol. **82**:985–994.

52. **Sosinsky GE, et al.** 2008. The combination of chemical fixation procedures with high pressure freezing and freeze substitution preserves highly labile tissue ultrastructure for electron tomography applications. J. Struct. Biol. **161**:359–371.

53. **Spilman MS, Welbon C, Nelson E, Dokland T.** 2009. Cryo-electron tomography of porcine reproductive and respiratory syndrome virus: organization of the nucleocapsid. J. Gen. Virol. **90**:527–535.

54. **Stertz S, et al.** 2007. The intracellular sites of early replication and budding of SARS-coronavirus. Virology **361**:304–315.

55. **Studer D, Michel M, Wohlwend M, Hunziker EB, Buschmann MD.** 1995. Vitrification of articular cartilage by high-pressure freezing. J. Microsc. **179**:321–332.

56. **Stueckemann JA, et al.** 1982. Replication of lactate dehydrogenase-elevating virus in macrophages. 2. Mechanism of persistent infection in mice and cell culture. J. Gen. Virol. **59**:263–272.

57. **Suhy DA, Giddings TH, Kirkegaard K.** 2000. Remodeling the endoplasmic reticulum by poliovirus infection and by individual viral proteins: an autophagy-like origin for virus-induced vesicles. J. Virol. **74**:8953–8965.

58. **Uchil PD, Satchidanandam V.** 2003. Architecture of the flaviviral replication complex. J. Biol. Chem. **278**:24388–24398.

59. **Ulasli M, Verheije MH, de Haan CAM, Reggiori F.** 2010. Qualitative and quantitative ultrastructural analysis of the membrane rearrangements induced by coronavirus. Cell Microbiol. **12**:844–861.

60. **van der Meer Y, van Tol H, Krijnse Locker J, Snijder EJ.** 1998. ORF1a-encoded replicase subunits are involved in the membrane association of the arterivirus replication complex. J. Virol. **72**:6689–6698.

61. **van Hemert MJ, de Wilde AH, Gorbalenya AE, Snijder EJ.** 2008. The *in vitro* RNA synthesizing activity of the isolated arterivirus replication/transcription complex is dependent on a host factor. J. Biol. Chem. **283**:16525–16536.

62. **van Hemert MJ, et al.** 2008. SARS-coronavirus replication/transcription complexes are membrane-enclosed and need a host factor for activity *in vitro*. PLoS Pathog. **4**:e1000054.

63. **Wada R, Fukunaga Y, Kondo T, Kanemaru T.** 1995. Ultrastructure and immuno-cytochemistry of BHK-21 cells infected with a modified Bucyrus strain of equine arteritis virus. Arch. Virol. **140**:1173–1180.

64. **Weber F, Wagner V, Rasmussen SB, Hartmann R, Paludan SR.** 2006. Double-stranded RNA is produced by positive-strand RNA viruses and DNA viruses but not in detectable amounts by negative-strand RNA viruses. J. Virol. **80**:5059–5064.

65. **Welsch S, et al.** 2009. Composition and three-dimensional architecture of the dengue virus replication and assembly sites. Cell Host Microbe **5**:365–375.

66. **Wieringa R, et al.** 2004. Structural protein requirements in equine arteritis virus assembly. J. Virol. **78**:13019–13027.

67. **Zeegers JJW, van der Zeijst BAM, Horzinek MC.** 1976. The structural proteins of equine arteritis virus. Virology **73**:200–205.